



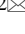




Geological and geostatistical analysis for equivalent uranium and thorium mineralization, Gattar-V Eastern Desert, Egypt

El Sayed A. Saber¹ , Ashraf Ismael^{2, 3} , Abdelrahem Embaby^{2*} , Yehia Z. Darwish^{2, 4} , Samir M. Selim² , Ehab Gomaa^{5, 6} , Ahmed A. Arafat^{5, 6} 

¹ Sohag University, Sohag, Egypt

² Al-Azhar University, Cairo, Egypt

³ Future University in Egypt, Cairo, Egypt

⁴ Nuclear Materials Authority, Cairo, Egypt

⁵ Suez University, Suez, Egypt

⁶ Taif University, Taif, Saudi Arabia

*Corresponding author: e-mail Abdel-raheemkhalifa.12@azhar.edu.eg

Abstract

Purpose. This paper aims to assess the distribution of uranium and thorium ore grade distribution to produce a uranium potential map and estimate of the uranium ore reserves in the Gattar-V area, Eastern Desert, Egypt.

Methods. Multidisciplinary approach is applied to determine the equivalent uranium mineralization in the Gattar-V area. It includes geological (petrographical, mineralogical and geochemical) and geostatistical (kriging analysis and variogram models) methods.

Findings. Geological studies show that the U-mineralization located along or near the contact between younger granites and Hammamat sediments exhibits episyenitization and bleaching alteration, respectively. Geochemical studies indicate a strong relationship between U-mineralization and Chemical Alteration Index (CIA), alteration features, and associated hydrothermal solution mineralization. The geostatistical method is used to study the behavior and distribution of U and Th in both younger granites and Hammamat sediments. The Total Gamma, eU, and eTh values are used in kriging analysis and variogram models to determine their spatial dependence and perform a spatial interpolation of sparse measurements and deposition level map.

Originality. The use of a multidisciplinary method combining petrographical, mineralogical and geochemical investigations with geostatistical analysis allowed for a quantitative evaluation of the spatial location of geological objects such as uranium mineralization in the area.

Practical implications. Variogram models and kriging analysis can also be used to assess the lithological composition of rocks and mineralogical phases, and they also provide a clear vision of the elements distributed in the ore, which is very useful during the planning and production stages.

Keywords: *Gattar-V, uranium mineralization, alteration, hydrothermal, kriging analysis, variogram models*

1. Introduction

Uranium and rare-metal mineralization occurs in different rock types of Egypt. As a component of the Precambrian basement complex in Egypt, granites are abundant in the Eastern Desert and Sinai [1]. Um Ara, El Sella Abu Rusheid, Sekait, El Erediya, Missikat and Gattar granites contain a variety of rare metals as well as uranium mineralization. In addition, uranium is associated with sedimentary rocks of Wadi Araba, Abu Zeneima, Black Sands (between Rashid and the city of Rafah on the Mediterranean coast of Egypt) and phosphate deposits (Abu Tartour).

The most significant mineralized rocks of Egypt are occurrences of Gattar granites (GII and GV) that host U-mineralization. Numerous workers are interested in these mineralized occurrences; the mineralized granites in the G. Gattar region are thought to contain up to 4000 tons of

uranium, according to Hussein and Sayyah [2]. According to Osmond et al. [3], secondary uranium ores in the Middle Eastern Desert were formed sporadically between 150000 and 60000 years ago; El-Feky [4] found that the temperature of mineralizing fluids ranges from 126 to 240°C; Salman et al. [5] demonstrate the connection between ascending hypogene solutions and uranium mineralization in the Gattar granite. According to El Zalaky [6], Roz [7], and Abdel Hamid [8], the geological contact zone between the Gattar younger granite and the Hammamat sedimentary strata is a favorable site for uranium mineralization.

An accurate surveying must be carried out immediately in order to identify areas with concentrated uranium mineralization and to comprehend the relationships between uranium mineralization and the ore-forming processes that can control these concentrations. Additionally, geostatistics is considered

Received: 25 July 2023. Accepted: 1 October 2023. Available online: 30 December 2023

© 2023, E.S.A. Saber et al.

Mining of Mineral Deposits. ISSN 2415-3443 (Online) | ISSN 2415-3435 (Print)

This is an Open Access article distributed under the terms of the Creative Commons Attribution License (<http://creativecommons.org/licenses/by/4.0/>), which permits unrestricted reuse, distribution, and reproduction in any medium, provided the original work is properly cited.

as an effective method for estimating and evaluating ore grade resources [9]-[11]. The purpose of the present work is to locate and map the uranium mineralization zones that are most likely or promising using a multidisciplinary approach based on geological, GIS and geostatistical data. The most important variables influencing uranium mineralization can be identified using lithology, uranium radiometry, chemical measurements, and the mineralogy of various alteration forms. The spatial distribution of eU, eTh, and Total Gamma radiation was described and mapped using geostatistical analysis. The GS+ 10 Geostatistical Analyst software was used to map the study area. The values of non-sampled places were interpolated using the kriging method. The purpose of the present work is to locate and map the uranium mineralization zones that are most likely or promising using a multidisciplinary approach based on geological, GIS and geostatistical data.

2. Geological setting

The study area is about 0.4 km². It is located between 27°07'00" N and 27°07'47" latitude and 33°16'50" E and 33°18'00" longitude and represents the northernmost part of the well-known Gattar granites.

According to geological investigations, the study area is composed of the Hammamat sedimentary rocks, acidic dikes, Gattar granites, basic dikes and Quaternary deposits. The rock units are arranged chronologically, starting with the oldest (Fig. 1). El Rakaiby and Shalaby [12] divide the batholith of Gattar younger granites into three phases, named G1, G2 and G3, based on their mode of occurrence and petrography. The Gabal Gattar pluton, considered in the current study, is from the youngest G3 phase. Contacts between granites and Hammamat sediment rocks (HSR) are often sharp with moderate metamorphism (Fig. 2a).

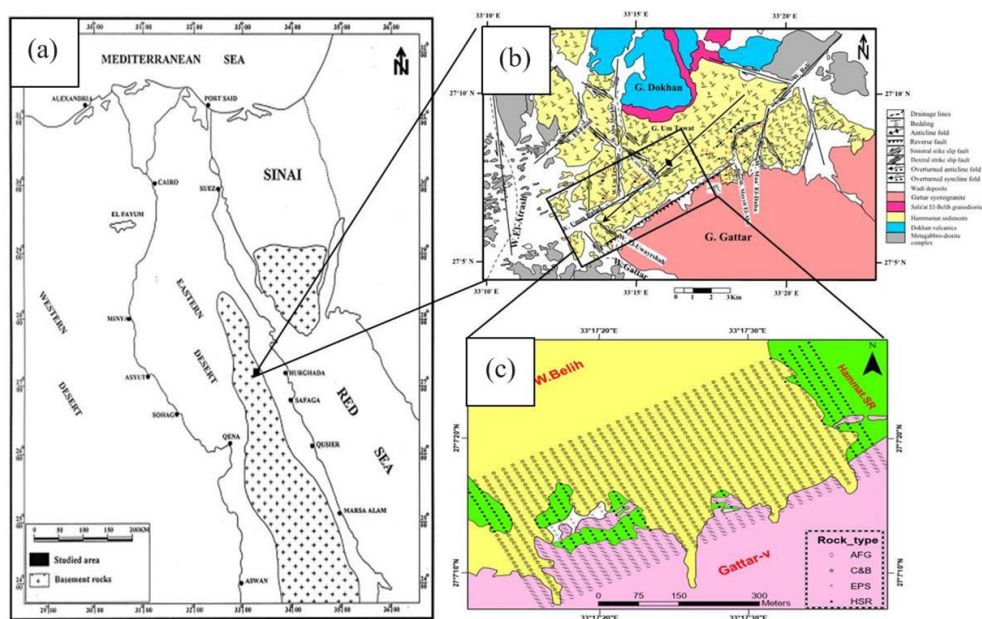


Figure 1. Geological maps of the study area: (a) the study area location; (b) geology; (c) locations of 1221 samples

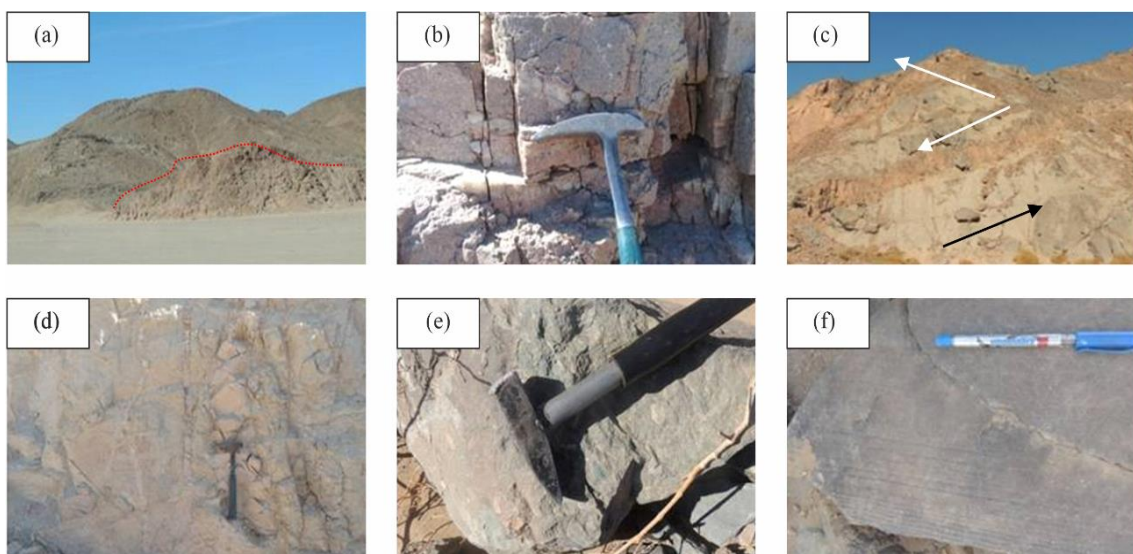


Figure 2. Field relation of the main rock units in the study area: (a) photograph showing contacts between the granites and Hammamat sediments; (b) alkali-feldspar granite ranges in color from pink to reddish pink; (c) basic and acidic dikes cutting the G. Gattar granite; (d) granite from the G. Gattar faults and fractures has quartz veins; (e) greywacke of Hammamat sediments; (f) laminated siltstone strata of Hammamat sediments

Alkali-feldspar granite represents both the southernmost part of the study area and the northernmost extremities of the G. Gattar pluton. In fairly recent samples, this rock ranges from pink to reddish pink (Fig. 2b), but it soon changes to become reddish brown or pale, especially close to the contact and fracture zones [8]. Basic dikes that fill fractures in the G. Gattar granite rupture it, while acidic dikes stop it when they come up against these rocks (Fig. 2c). Along the contact between Hammamat sediments and younger granite, several quartz veins can be seen. Quartz veins occur around faults and fractures (Fig. 2d), which are responsible for silicification of the host rocks [7]. The study area is covered by Hammamat sediment rocks (HSR) in the north, while in the center they are visible only as individual outcrops. Hammamat sediments are primarily composed of greywacke (Fig. 2f), alternated with thinly stratified siltstone present along their southern boundary where they contact granite. They have undergone significant alteration, being foliated, laminated (Fig. 2f), fractured and faulted, especially where they contact the granite [8], [13], [14].

3. Material and methods

The work is divided into field and laboratory work. Field work includes describing and measuring the major mineralization location, representative samples of mineralization of host rocks and mineral deposits, collected for petrographical and geochemical examinations. Laboratory work includes preparation of samples for petrographical, mineralogical and geochemical investigations. More than 25 thin sections have been prepared for microscopic analysis using a polarizing microscope in transmitted and reflected light. Geochemical analyses are performed on 32 samples of younger granite rocks and 15 samples of Hammamat sediments for major and trace elements composition (in wt % and ppm, respectively). Geochemical investigation is conducted using a Philips X-ray fluorescence technique of PW/2404 type with Rh radiation tube. While detection limits for major composition range from 0.001 to 0.03% and 0.5 ppm for loss on ignition (L.O.I.), the detection limits for trace element levels range from 0.01 to 0.5 ppm. All geochemical analyses are carried out by the Central Laboratories of the Geological Survey of Egypt.

Statistical analysis, performed with a portable calibrated Gamma-Ray spectrometer model RS-230, is used for eU (ppm) detection and is the basis for ground-based gamma-ray spectrometry measurements. Using 1221 points from the above grid pattern (Fig. 1c), GS+ 10 Geostatistical Analyst software is used to perform statistical analysis, build a variogram model, and create kriged maps of distribution.

4. Results

4.1. Petrography of U-host rocks

4.1.1. Granite

In hand samples, young granite appears medium to coarse-grained and ranges in color from whitish-pink to red, while certain samples, especially mineralized ones, are reddish-brown in color. According to ElSayed [15], the reddish-brown color of younger granite may be due to the presence of dusty hematite in the K-feldspar. Under the microscope, younger granite is mostly composed of quartz, which accounts for 30%, potash feldspar – 35%, plagioclase – 26% (Fig. 3a, b), while a mafic phase consists mainly of biotite and chlorite, which accounts for less than 5% (Fig. 3c). The most common inclusions are fluorite, zircon, xenotime, monazite, apatite and sphene, while secondary minerals are allanite, uraninite, and uranophane (Fig. 3d, e). Besides chalcopyrite and pyrrhotite, opaque minerals include ilmenite, magnetite, pyrite, and goethite (Fig. 3f).

4.1.2. Hammamat sediments

Greywacke is black to grey in color, fine-grained to coarse-grained, and immature (Fig. 4a). The clasts consist of quartz grains with sub-angular to sub-rounded outlines, altered feldspars, rock fragments, and a matrix of about 20-40%, which contains a lot of fine-grained quartz, iron oxide, secondary minerals of sericite, chlorite and locally calcite. Quartz often occurs as polycrystalline aggregates about 2 mm in size (Fig. 4b), sometimes have a mosaic texture. Monocrystalline quartz is rare or absent. Feldspar is mainly represented by suritized plagioclase (Fig. 4c) and occurs as subhedral to anhedral grains. Rock fragments are abundant and mainly represented by granitic rock fragments, other types of rock fragments such as acidic volcanic (Fig. 4c) and quartzite.

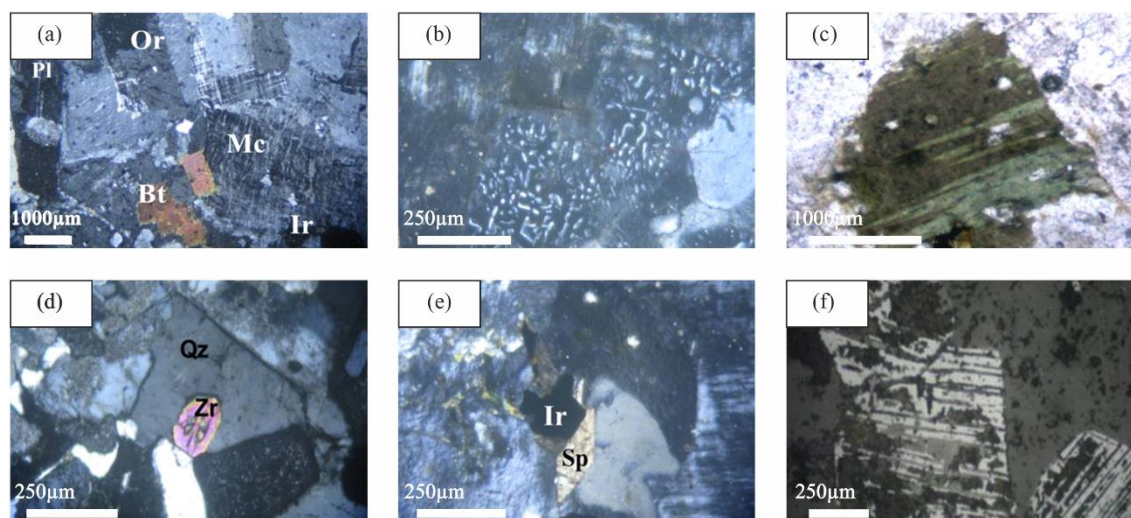


Figure 3. Photomicrographs showing the Petrography of Gattar younger granite: (a) microcline perthite (Mc), quartz (Qz), and plagioclase (Pl), as well as smaller amounts of biotite (Bt), sphene (Sph), and iron oxide (Ir), make up the hypidiomorphic texture of alkali granite (C.N.); (b) vermicular intergrowth between quartz and plagioclase feldspar forming myrmekitic texture (C.N.); (c) chlorite replacing biotite (C.N.); (d) euhedral prismatic crystal of zircon (Zr) inside quartz (Qz) (C.N.); (e) rhombic sphene (Sp) crystal surrounded by iron oxides (Ir) (C.N.); (f) photomicrograph display intergrowth between Ilmenite and magnetite crystals (RL), μm

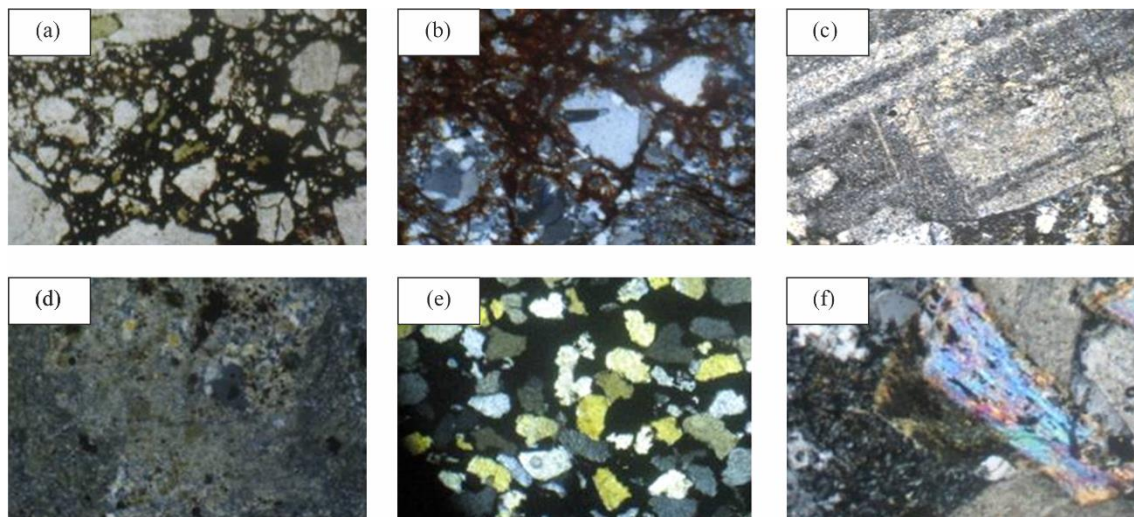


Figure 4. Photomicrographs showing the petrography of Hammamat sediments: (a) photomicrograph showing greywackes composition, investigated Hammamat sediments; (b) photomicrograph showing polycrystalline quartz aggregates in greywacke; (c) photomicrograph showing greywacke partially saussuritized by plagioclase; (d) photomicrograph showing occurrences of acidic volcanic rock fragments in greywacke; (e) siltstone composed of angular to sub-rounded quartz grains; (f) photomicrograph showing the occurrences of detrital mica in siltstones

Siltstones under a microscope, where the siltstone fraction is represented by fine angular to sub-rounded quartz grains, which make up siltstones (Fig. 4e). Feldspar, detrital mica, microcrystalline chlorite, sericite (Fig. 4f), and epidote are tightly confined to a hematite matrix. Rock fragments are relatively rare, while feldspars are rounded or sub-rounded. There are no veinlets or areas of carbonate.

4.2. Geochemistry of U-host rocks

4.2.1. Granite

In order to categorize plutonic igneous rocks based on various geochemical parameters, several diagrams are used. Cox et al. [16] use $(\text{Na}_2\text{O} + \text{K}_2\text{O})$ vs. SiO_2 diagram to categorize plutonic igneous rocks. By applying this diagram, samples of current granitic rocks falling within the alkali granite are plotted (Fig. 5a). The examined granitic rocks are sub-alkaline by affinity, according to Irvine and Baragar [17], who use the $(\text{Na}_2\text{O} + \text{K}_2\text{O})$ - SiO_2 diagram to mark the alkaline and sub-alkaline rock nature (Fig. 5b). Peccerillo and Taylor [18] use K_2O vs. SiO_2 diagram to differentiate the low-K (tholeiite), calc-alkaline, high-K (calc-alkaline), and shoshonite series. The plots of the present granitic samples belong to the high-K (calc-alkaline) series (Fig. 5c). Except for EPS, the samples of younger granite show variable series due to the alteration effects.

The Na_2O vs. K_2O diagram was put forward by Chappell and White [19] to see the difference between I-type and S-type granites. Granitic sample plots are located in the I-type field (Fig. 5d). Except for some EPS samples, the younger granite shows S-type under the effects of alteration. The SiO_2 -Rb diagram was suggested by Pearce et al. [20] to distinguish between various geological tectonic environments. With the exception of EPS samples, plotting of the present younger granite samples reveals that they decline in the Syn-collision granite (Syn-COLG) field (Fig. 5e). EPS samples decline in the volcanic arc granite (VAG) field. This shift may be due to alteration. Maniar and Piccoli [21] FeOt vs. MgO diagram also shows that the plots of granitoid rock samples fall into the CAG + IAG + CCG field (continental arc granite + island arc granite + continental collision granitoids) (Fig. 5f).

4.2.2. Hammamat sediments

Geochemical classification. Using sediment geochemical classification diagrams, $\text{Log}(\text{Na}_2\text{O}/\text{K}_2\text{O})$ vs. $\text{Log}(\text{SiO}_2/\text{Al}_2\text{O}_3)$ of [22], all presented samples refer to the greywacke field (Fig. 6a). Using the $\text{Log}(\text{Fe}_2\text{O}_3/\text{K}_2\text{O})$ vs. $\text{Log}(\text{Na}_2\text{O}/\text{K}_2\text{O})$ infographic [23] (Fig. 6b), the majority of Hammamat sediment samples are plotted in the greywacke field. These results indicate the same origin of the studied samples.

Geochemical evidence of provenance. The geochemical data on terrigenous rocks may be used to provide information about their origin. The examined samples of the Hammamat sedimentary rocks belong to the felsic and intermediate provenances, according to a plot of Hammamat sediments on the V-Ni-Th*10 ternary diagram [24] (Fig. 7).

Geological tectonic environments of the Hammamat sedimentary rocks studied in the present work are depicted using $\text{Log}(\text{K}_2\text{O}/\text{Na}_2\text{O})$ vs. SiO_2 diagram [25]. Figure 8 analyzes main samples located within the active continental margin field. Bhatia in [26] distinguishes the geological and tectonic environments of the sedimentary rocks based on the major element compositions. Most of the examined Hammamat sediments samples are located inside or near the continental island arc field [26] (Fig. 9a, b).

4.3. Uranium mineralization

The Gattar granite pluton-uranium mineralization is related to vein-type mineralization associated with molybdenite, where the mineralization is generally elongated in the direction of the main fracture zone. Mineralization occurs along microfracture surfaces (Fig. 10a, b), coating cavities (Fig. 10c), vugs (Fig. 10d), and in the form of thin films and small clots (Fig. 10e, f). Black fluorite, iron oxides, and manganese oxides are always present with uranium ore deposits. Visible secondary uranium minerals are the main representatives of the uranium mineralization and include soddyite and uranophane with finely dispersed sooty pitchblende.

The uranium mineralization, hosted in the Hammamat sediments, is mainly visible secondary uranium mineralization. The secondary uranium minerals are mainly associated with the altered mineralized Hammamat sediments (Fig. 10g).

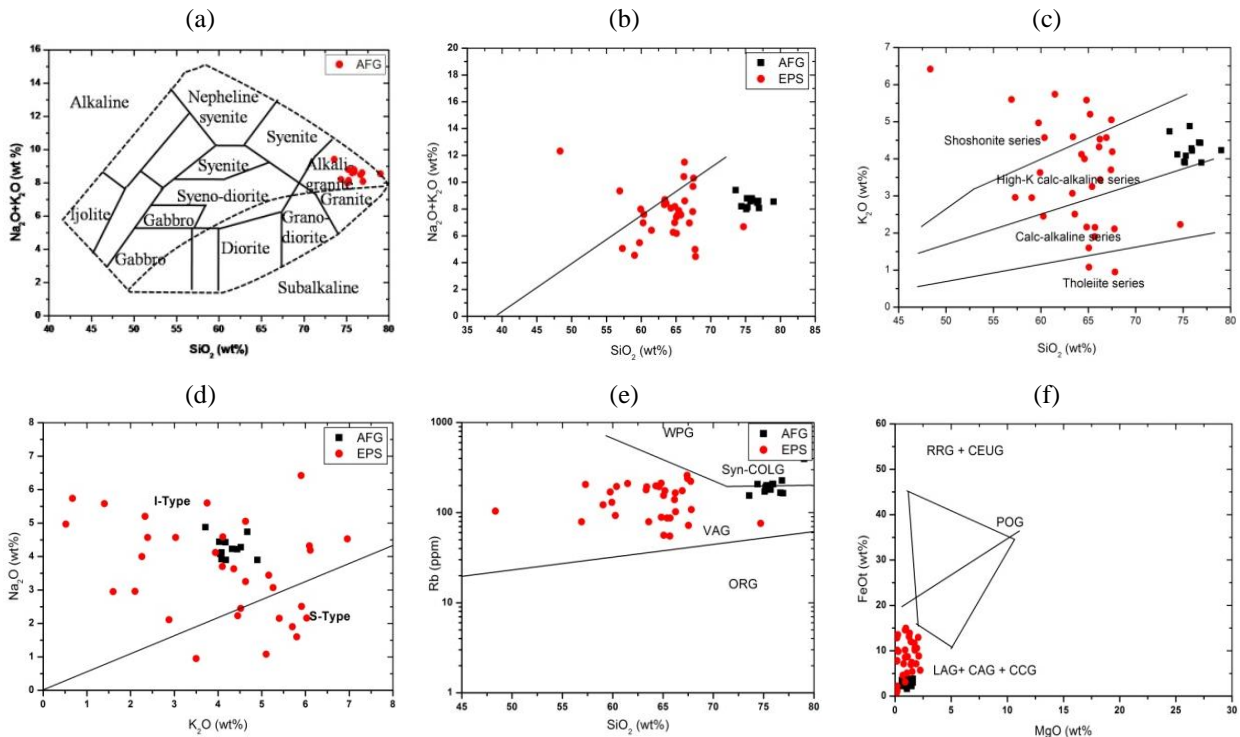


Figure 5. Geochemical discrimination plots of intrusive younger granite: (a) plots of the investigated intrusive rocks on the SiO_2 ($Na_2O + K_2O$) diagram of Cox et al. (1979); (b) plots of the present intrusive rocks on the SiO_2 vs. $K_2O + Na_2O$ diagram of Irvine and Baragar (1971); (c) plots of the present granitic rocks on the K_2O vs. SiO_2 diagram of Peccerillo and Taylor (1976); (d) plots of the present granitoids samples on the Na_2O vs. K_2O diagram of Chappell and White (1974); I-type – igneous, S-type – sedimentary; (e) plots of the present granite samples on the SiO_2 -Rb diagram of Pearce et al. (1984); VAG – volcanic arc granite; ORG – oceanic ridge granite; Syn-COLG – syn-collision granite; WPG – within plate granite; (f) plots of the investigated granites on the FeO - MgO diagram of Maniar and Piccoli (1989); IAG – island arc granite; CCG – continental collision granitoids; CAG – continental arc granite; POG – post orogenic granites; RRG – rift-related granitoids; CEUG – continental epeirogenic uplift granitoids

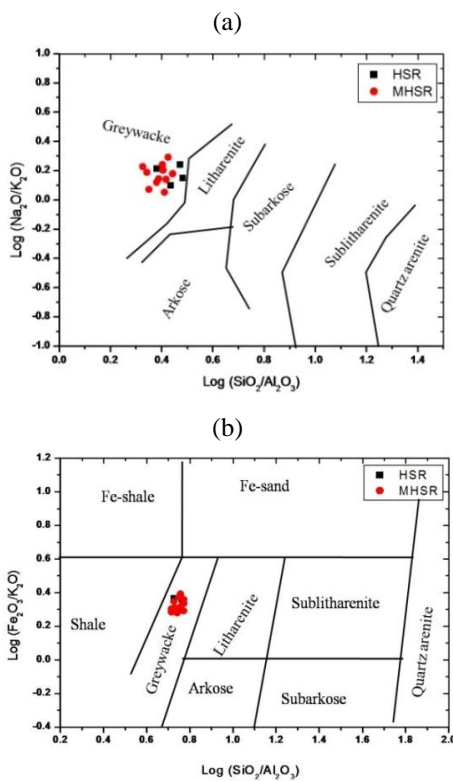


Figure 6. Geochemical classification of Hammamat sediments: (a) $\text{Log} (Na_2O/K_2O)$ vs. $\text{Log} (SiO_2/Al_2O_3)$ classification diagram of terrigenous sandstone types [22]; (b) $\text{Log} (Fe_2O_3^*/K_2O)$ vs. $\text{Log} (SiO_2/Al_2O_3)$ classification diagram of terrigenous sandstone types [23]

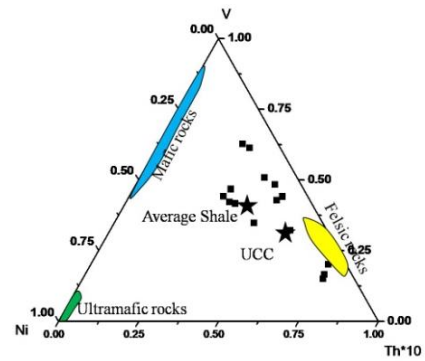


Figure 7. Geochemical plot showing provenance of Hammamat sediments, plotting Hammamat sediments on V-Ni-Th*10 diagram [24]

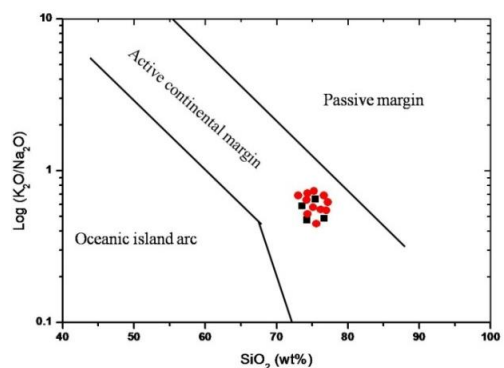


Figure 8. Geological tectonic environments of the Hammamat sedimentary rocks, $\text{Log} (K_2O/Na_2O)$ vs. SiO_2 diagram [25] for the studied Hammamat sedimentary rocks

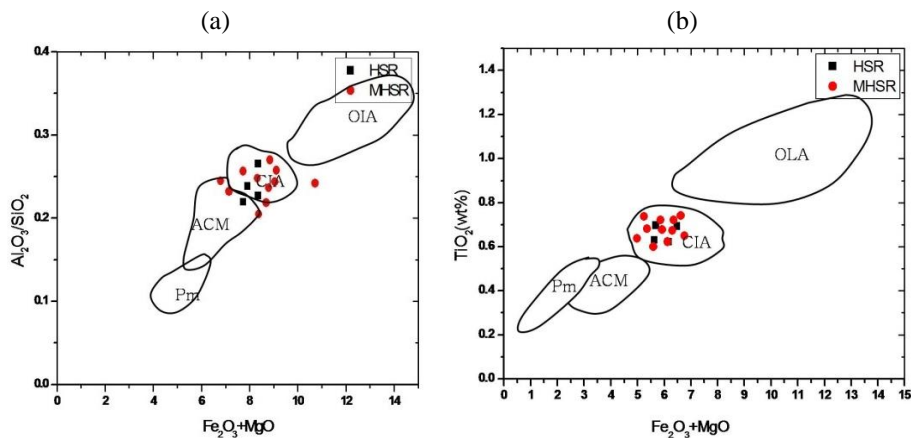


Figure 9. Geological tectonic environments of the Hammamat sedimentary rocks: (a) TiO_2 vs. $(Fe_2O_3^* + MgO)$ discrimination diagrams for the studied Hammamat sedimentary rocks [26]; (b) Al_2O_3/SiO_2 vs. $(Fe_2O_3^* + MgO)$ discrimination diagrams for the studied Hammamat sedimentary rocks; OIA – oceanic island arcs; CIA – continental island arcs; ACM – active continental margins; PM – passive margins

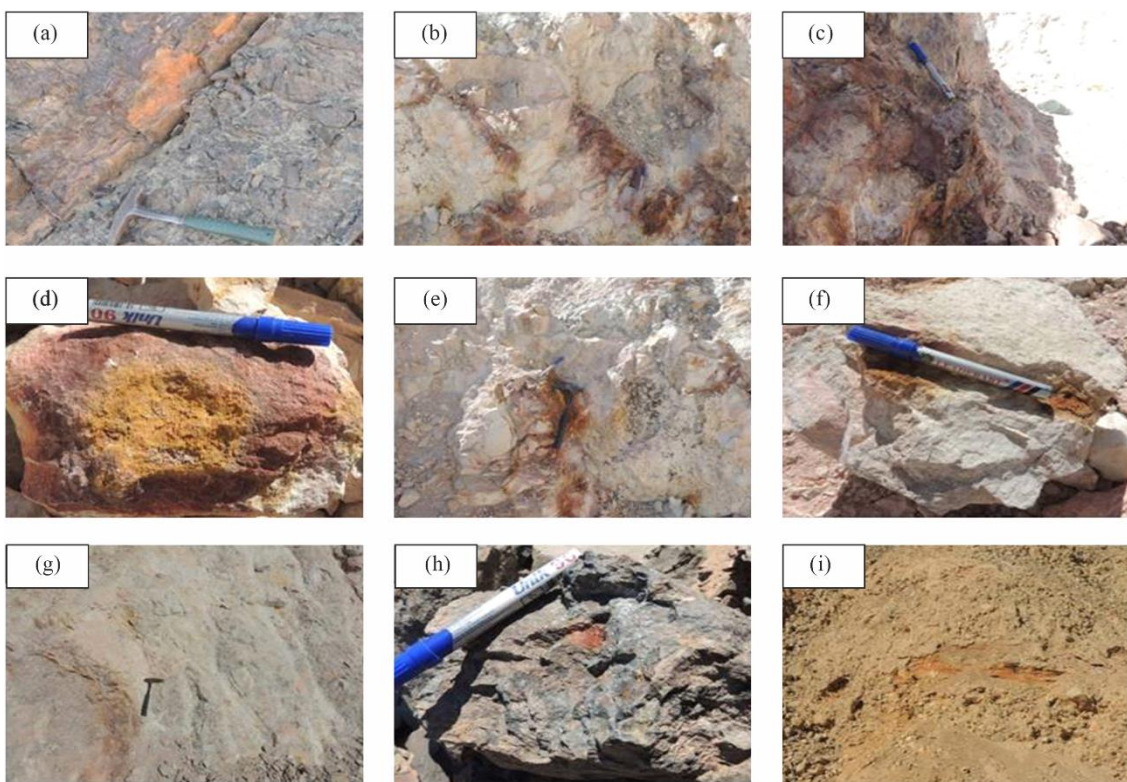


Figure 10. Field photographs of uranium mineralization at Gattar granite and Hammamat sediment: (a) and (b) uranium mineralization at Gattar granite pluton occurs along micro-fracture surfaces; (c) uranium mineralization at Gattar granite pluton occurs as coating in cavities; (d) uranium mineralization at Gattar granite pluton occurs as vug filling; (e) and (f) uranium mineralization at Gattar granite pluton occurs as thin films and fine clots; (g) altered mineralized Hammamat sediments; (h) secondary uranium mineralization coating in Hammamat sediments; (i) secondary uranium mineralization in bleached siltstone strata

The mineralization is represented by uranophane and beta-uranophane, which occur in the form of coating along fractures and lineations of the Hammamat sediments (Fig. 10h). The minerals form acicular needles and small bundles of yellow color [27]. This mineralization is mainly concentrated on bleached siltstone strata (Fig. 10i) [28].

4.4. Geostatistical analysis

4.4.1. Ordinary kriging (OK)

Ordinary kriging is a common multidimensional interpolation method $\hat{y}(x_0)$ in which the value of the variable y at a specific location x is predicted from known sample values $\{(x_i, y_i)\}_{i=1}^m$ [29].

$$\hat{y}(x_0) = \sum_{i=1}^m \lambda_i y(x_i), \tag{1}$$

where:

$\hat{y}(x_0)$ – kriging prediction at unknown location;

$x_0; y(x_i)$ – known value at location x_i and λ_i weighting factor for $y(x_i)$.

The kriging prediction error is:

$$\hat{y}(x_0) - y(x_0) = R(x_0) = \sum_{i=1}^m \lambda_i y(x_i) - y(x_0), \tag{2}$$

where:

$y(x_0)$ – unknown true value at x_0 ;

$R(x_0)$ = prediction error. For an unbiased estimate, the average prediction error must be equal to zero, hence:

$$E\{R(x_0)\} = 0, \tag{3}$$

and

$$\sum_{i=1}^m \lambda_i = 1. \tag{4}$$

The reader is referred to the literature for more information on the ordinary kriging method and its use [30].

4.4.2. G-V statistical and geostatistical analysis and mapping

Statistical analysis of presented data. The statistical analysis as presented in Table 1 shows the statistical description of the data, where eU ranges from 0.4 to 37.9 ppm, eTh ranges from 5 to 38.9 ppm, and Total Gamma ranges from 140 to 349 cpc. Figure 11 indicates that the eU is directly proportional to eTh with regression coefficient 1.27 and r^2 0.691.

Table 1. Summary statistics of the datasets used in the study area

Statistical parameters	Equivalent Thorium	Equivalent Uranium	Total Gamma
Average	21.255	12.748	227.099
Std. deviation	8.12	5.312	50.78
Sample variance	65.93	28.218	2578.56
Min. value	5	4	140
Max. value	38.9	37.9	349
Sample number	1221	1221	1221
Skewness	-0.03	1.05	0.63
Kurtosis	-0.84	3.05	-0.4

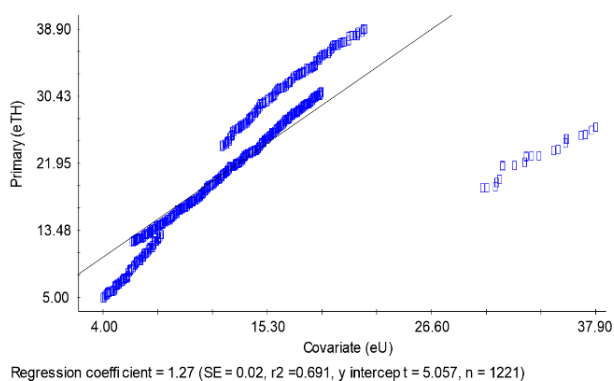
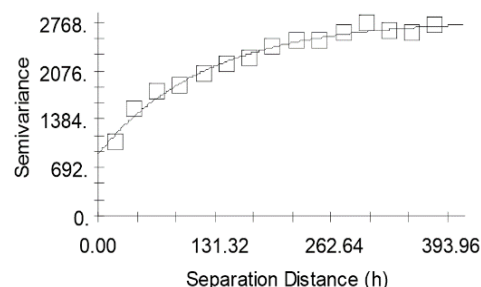


Figure 11. Relationships between eU and eTh

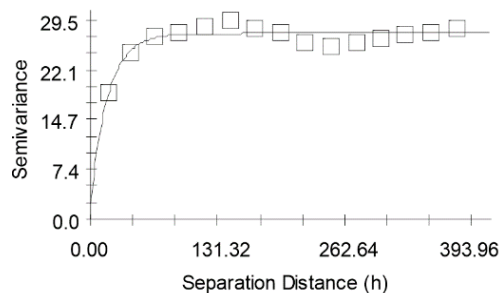
In statistics, linear regression is a linear approach to modeling the relationships between a scalar response and one or more explanatory variables (also known as dependent and independent variables) eTh and eU, respectively, as shown in Figure 11. In linear regression, the relationships are modeled using linear predictor functions whose unknown model parameters are estimated from the data. The goal is to reduce errors in prediction. Linear regression can be used to fit a predictive model to an observed data set of response values and explanatory variables. After developing such a model, as indicated in Figure 11, if additional explanatory variable values are collected without an accompanying response value, the fitted model can be used to predict the response.

Geostatistical analysis and mapping. Variograms construction. Variogram is the first step in any geostatistical study and has a vital role in ore evaluation process. The selected variogram model will be used in the kriging calculation and will affect all results and conclusions. Global variogram is constructed for Total Gamma, eU and eTh depending on the available data for each parameter. An exponential model is selected as more suitable model for all of them with r^2 0.98, 0.835 and 0.983, respectively, as shown in Figures 12-14.



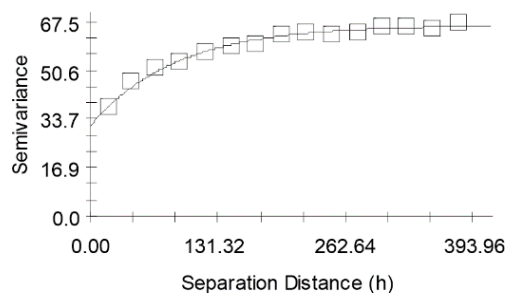
Exponential model ($C_0 = 890.00000$; $C_0 + C = 2802.00000$; $A_0 = 123.10$; $r^2 = 0.980$; $RSS = 69468$.)

Figure 12. Total Gamma variogram model



Exponential model ($C_0 = 2.35000$; $C_0 + C = 27.52000$; $A_0 = 18.00$; $r^2 = 0.835$; $RSS = 14.7$.)

Figure 13. e Uranium variogram model



Exponential model ($C_0 = 31.51942$; $C_0 + C = 66.50000$; $A_0 = 88.60$; $r^2 = 0.983$; $RSS = 21.0$.)

Figure 14. e Thorium variogram model

The variogram parameters for Total Gamma, eU, and eTh in the study area are summarized in Table 2.

Table 2. Variogram parameters of the datasets used in the study area

Variogram parameters	T Gamma cpc	eU ppm	eTh ppm
Type	Exponential		
Direction	Global		
Range, m	123.1	18	88.6
Nugget effect (C_0), % ²	890	2.35	31.52
Sill ($C + C_0$), % ²	1912	25.17	34.98
Screen effect ratio C_0/C	0.47	0.09	0.9

Each variogram model has its own special parameters that describe the variability of Total Gamma, eU, and eTh within the study area, as shown in Figures 12-14, respectively. These variogram parameters are very important and are used when creating kriging models (in Section 5) for mapping analysis (Fig. 17a-c) that reveals the spatial distribution of Total Gamma, eU, and eTh. These parameters are summarized in Table 2.

5. Discussion

Based on the geological setting, the examined U-mineralization was found near the boundary between younger granite and the Hammamat sedimentary rocks [7], [14], [31], [32]. Hydrothermal solutions affecting the examined rock types result in numerous changes that are typically present along and near the boundaries between them [7], [8]. Strong hematite, bleaching, fluorite, together with carbonate, kaolinite, and some manganese minerals are the prevalent alteration products of the Hammamat sedimentary rocks. The most frequent minerals formed in the wall-rock alteration of granitic rocks are manganese, episyenites, hematite, secondary silica, kaolinite, chlorite, and fluorite.

The $(\text{Na}_2\text{O} + \text{CaO}) - \text{Al}_2\text{O}_3 - \text{K}_2\text{O}$ triangular diagram [33], [34] shows the weathering tendencies. The relative alteration of the studied mineralized samples is evident in the alteration of feldspars to clay minerals and results in the enrichment of the altered samples with K_2O and Al_2O_3 [35], [36] (Fig. 15a). In Figure 15b, samples of unaltered and altered granite and

Hammamat sediments are plotted on the AKF ternary diagram of Meyer et al. [37]. It demonstrates that all samples of altered granites and Hammamat sediments belong to the propylitic field and sericite facies as a result of the sericitization processes.

Large changes in Na, Ca, Mg, and Fe contents are among the most obvious geochemical features of U-rich samples [38]. Na_2O and CaO gradually decrease as alteration intensity increases, reaching a point where samples with extreme alteration have $\text{Na}_2\text{O} + \text{CaO}$ percentage values. This pattern is suggestive of the breakdown of plagioclase and the emergence of muscovite/sericitization (Fig. 15c) [39].

The majority of the features of uranium alteration and mineralization are closely related. Figure and graph of U vs. CIA and Th vs. CIA indicate that both U and Th concentrations increase with increasing chemical alteration (Fig. 15d, e). Using the U vs. Th relation, two distinct trends emerge. Magmatic and fluid fractionation trends can be shown in the Gattar granite (Fig. 15f).

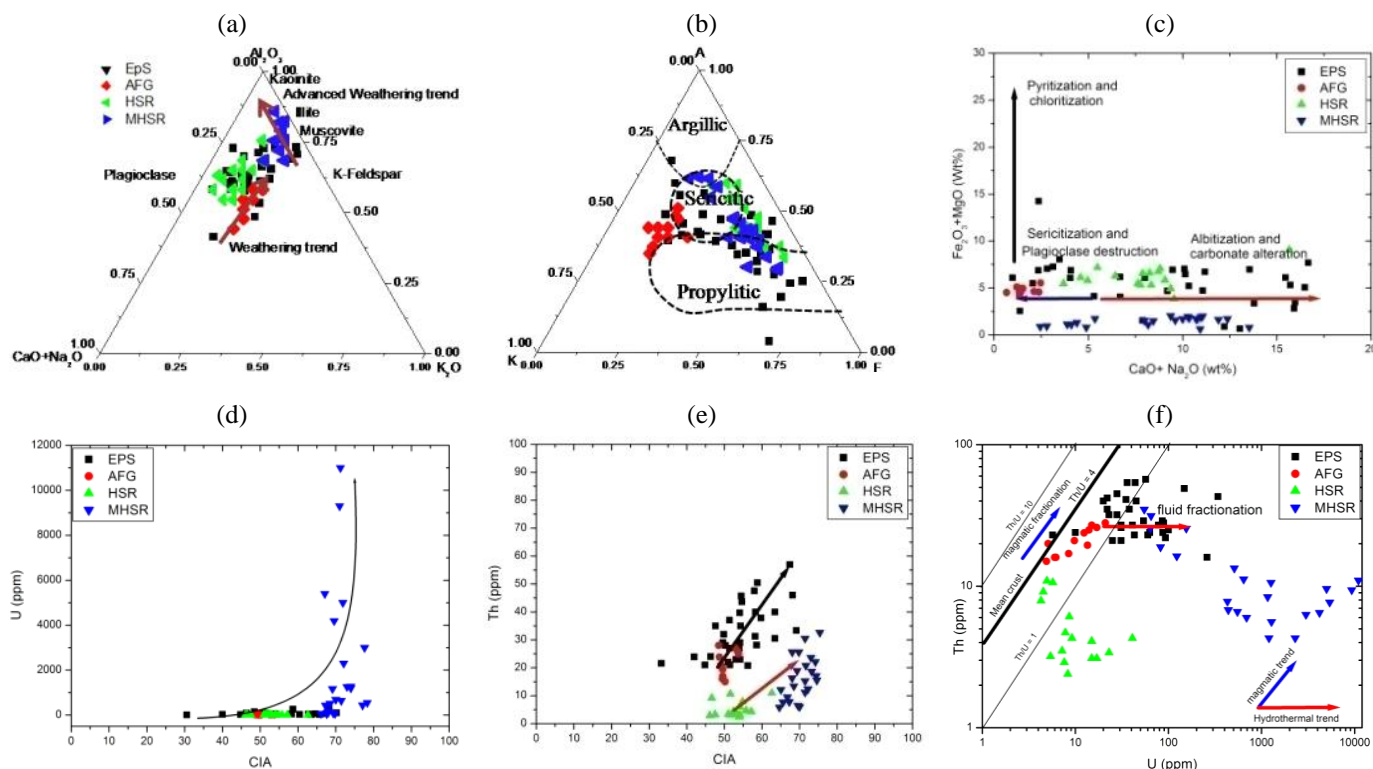


Figure 15. Alteration of younger granites and Hammamat sediments and their relation to uranium mineralization: (a) $\text{Al}_2\text{O}_3 - (\text{CaO} + \text{Na}_2\text{O}) - (\text{K}_2\text{O})$ diagram of younger granites and Hammamat sediments; (b) AKF ($A = \text{Al}_2\text{O}_3 - (\text{Na}_2\text{O} + \text{K}_2\text{O})$, $K = \text{K}_2\text{O}$, and $F = \text{FeO} + \text{MnO} + \text{MgO}$) ternary diagram of younger granites and Hammamat sediments; (c) alteration factors for younger granites and Hammamat sediments; (d) U vs. CIA for younger granites and Hammamat sediments; (e) U vs. Th for younger granites and Hammamat sediments; (f) Th vs. U for younger granites and Hammamat sediments

These two trends show that there are fluid phases that influence U-mineralization in magmatic and late- to post-magmatic processes [40].

According to Cuney and Kyser [41], uranothorite and other related accessory minerals are the main factors that regulate the quantity of uranium enrichment in A2 type high-K calc-alkaline granites such as Gattar granite. Gattar granite, however, does not contain this mineral. Mahdy [42] studied the Gattar granite and concluded that U+4 replaced Zr along rims of zircon crystals at the late magmatic stage.

The alteration box (AI vs. CCPI) is a valuable tool for separating geochemical trends caused by hydrothermal alteration from those that can be attributed to diagenetic alteration [43]. Gattar granite samples (Fig. 16a) are found only with sericite-pyrite-chlorite, chlorite-pyrite, and carbonate-sericite patterns of hydrothermal alteration, which indicates to the influence of hydrothermal solution on the U-ore formation in the study area. The U-Zr-Si ternary diagram [44] illustrates the composition of uranium minerals from Gattar-V. “Uranoan zircon” refers to an early primary phase altered under the influence of hydrothermal solution to a secondary phase ending in uraninite (Fig. 16b).

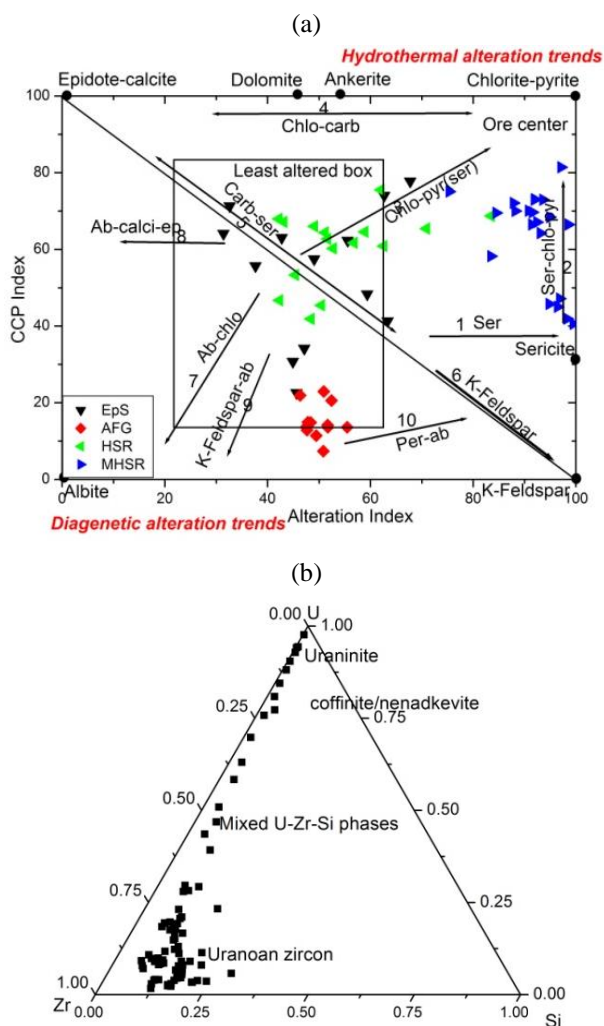


Figure 16. Alteration of younger granites and Hammamat sediments and their relation to uranium mineralization: (a) boxplot diagram of alteration for Gattar granite and Hammamat sediments ($AI = 100 (K_2O + MgO) / (K_2O + MgO + Na_2O + CaO)$ and $CCPI = 100 (MgO + FeO) / (MgO + FeO + Na_2O + K_2O)$); (b) Si-U-Zr Ternary diagram illustrating the compositional range of uranium minerals from the Gattar granite and Hammamat sediments

Ordinary Kriging was used to interpolate non-sampled locations by creating a map analysis that shows the spatial distribution of Total Gamma, eU, and eTh in the study area, as shown in Figure 17a-c, depending on the selected variogram model for each of them.

Maps are classified by colour, and each colour represents a definite range of percentage for Total Gamma, eU, and eTh, as shown in Figure 17a-c. The low percentage of Total Gamma, eU, and eTh are located on the border of NE and SW directions of the study area. On the other hand, the high percentage of Total Gamma and eTh is in the NE-SW direction in the lower part of the study area. The high ratio of eU is disseminated in the lower part and SW direction of the area. While a moderate ratio for all of them is common in the upper and central parts of the study area.

The obtained results from multidisciplinary approach using integrated geological and geostatistical data to get uranium potential map of the study area can provide useful information. This information will guide planning of mining activity and sound decision-making regarding uranium resource.

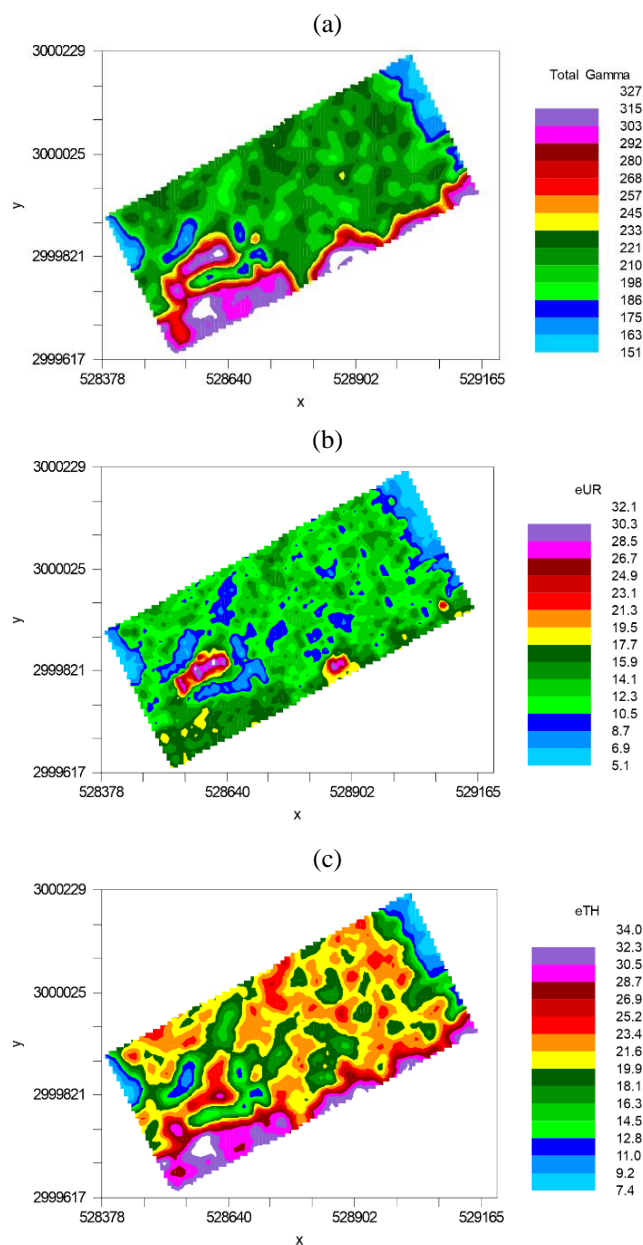


Figure 17. Kriged maps: (a) Total Gamma; (b) e Uranium; (c) e Thorium

6. Conclusions

U-mineralization in the Gabal Gattar area was found near the boundary between younger granite from the Late Neoproterozoic and the Late Precambrian Hammamat sedimentary. Major mineralization is structurally controlled, especially along the shear zone striking ENE-WSW to NE-SW direction.

The numerous alterations presented are associated with uranium mineralization along and near the boundary of younger granites and the Hammamat sedimentary rocks. These are mainly episyenites, hematitization, silicification, kaolinitization, fluoritization, epidotization and manganese dendrites, which are the most pronounced wall rock alterations associated with granite alteration. In this case, the alteration features are associated with hematitization, kaolinitization, epidotization, fluoritization, chloritization, manganese dendrites and bleaching of Hammamat sediments. Most alteration features and uranium mineralization are closely related.

U-mineralization is influenced by both magmatic and late-to post-magmatic fluid phases. These fluids are classified as

hydrothermal solutions, and the later play significant role in the formation of the secondary phase of U-mineralization.

Kriging analysis and variogram modeling of Total Gamma, eU, and eTh values were used to determine their spatial dependence, perform spatial interpolation of sparse measurements, and calculate map of deposition levels.

The geological survey confirms geostatistical findings from the kriging analysis that there is a concentration of U-mineralization on the boundary between younger granites and Hammamat sediments.

Kriging analysis and variogram models can also be used to evaluate the lithological composition of rocks and mineralogical phases. They also give a clear picture of the elemental distribution in the ore, which is particularly useful during the planning and production stages.

References

- Ali, B.H., Wilde, S.A., & Gabr, M.M.A. (2009). Granitoid evolution in Sinai, Egypt, based on precise SHRIMP U-Pb zircon geochronology. *Gondwana Research*, 15(1), 38-48. <https://doi.org/10.1016/j.gr.2008.06.009>
- Hussein, H.A.M., & Sayyah, T.A. (1992). *Uranium potential of the younger granites of Egypt*. Report No. IAEA-TECDOC-650.
- Osmond, J.K., Dabous, A.A., & Dawood, Y.H. (1999). U series age and origin of two secondary uranium deposits, central Eastern Desert, Egypt. *Economic Geology*, 94(2), 273-280. <https://doi.org/10.2113/gsecongeo.94.2.273>
- El Feky, M.G., El Mowafy, A.A., & Abdel Warith, A. (2011). Mineralogy, geochemistry, radioactivity and environmental impacts of Gabal Marwa granites, southeastern Sinai, Egypt. *Chinese Journal of Geochemistry*, (30), 175-186. <https://doi.org/10.1007/s11631-011-0499-1>
- Salman, A.B. (1986). New occurrence of uranium mineralization in Gabal Gattar, North Eastern Desert, Egypt. *Annals of Geological Survey of Egypt*, 31-34.
- El Zalaky, M.A. (2018). Uranium potentiality mapping of GV occurrence at Gabal Gattar area, North Eastern Desert, Egypt, using GIS approach. *Beni-Suef University Journal of Basic and Applied Sciences*, 7(4), 547-558. <https://doi.org/10.1016/j.bjbas.2018.06.007>
- Roz, M.E. (1994). *Geology and uranium mineralization of Gabal Gattar area, North Eastern Desert, Egypt*. M.Sc. Thesis. Cairo, Egypt: Al-Azhar University, 175 p.
- Abdel Hamid, A.A. (2006). *Geologic factors controlling the radon emanation associated with uranium mineralization along Wadi Belih, NED, Egypt*. M.Sc. Thesis. Benha, Egypt: Benha University, 189 p.
- Samanta, B., Bandopadhyay, S., & Ganguli, R. (2006). Comparative evaluation of neural network learning algorithms for ore grade estimation. *Mathematical Geology*, (38), 175-197. <https://doi.org/10.1007/s11004-005-9010-z>
- Abu Bakarr, J., Sasaki, K., Yaguba, J., Karim, B.A., (2016). Integrating artificial neural networks and geostatistics for optimum 3D geological block modeling in mineral reserve estimation: A case study. *International Journal of Mining Science and Technology*, 26(4), 581-585. <https://doi.org/10.1016/j.ijmst.2016.05.008>
- Embaby, A., Ismael, A., Ali, A.F., Farag, H.A., Mousal, B.G., Gomaa, S., & Elwageeh, M. (2023). An approach based on machine learning algorithms, geostatistical technique, and GIS analysis to estimate phosphate grade at the Abu Tartur Mine, Western Desert, Egypt. *Mining of Mineral Deposits*, 17(1), 108-119. <https://doi.org/10.33271/mining17.01.108>
- El Rakaiby, M.L., & Shalaby, M.H. (1992). Geology of Gebel Qattar batholith, Central Eastern Desert, Egypt. *International Journal of Remote Sensing*, 13(12), 2337-2347. <https://doi.org/10.1080/01431169208904272>
- Khalifa, A.A., Khamis, H.A., El-Sayed, M.M., & Shalaby, M.H. (2020). Geology and evolutionary stages of the Late Precambrian Hammamat sediments at Gebel Um Tawat, North Eastern Desert, Egypt. *Arabian Journal of Geosciences*, (13), 1-19. <https://doi.org/10.1007/s12517-020-05323-9>
- Abu Zaid, M.M. (1995). *Relation between surface and subsurface uranium mineralization and structural features, Gebel Gattar, North Eastern Desert, Egypt*. M.Sc. Thesis. Cairo, Egypt: Ain Shams University, 17 p.
- El-Sayed, M.M., Mohamed, F.H., Furnes, H., & Kanisawa, S. (2002). Geochemistry and petrogenesis of the Neoproterozoic granitoids in the Central Eastern Desert, Egypt. *Geochemistry*, 62(4), 317-346. <https://doi.org/10.1078/0009-2819-00010>
- Cox, K.G., Bell, J.D., & Pankhurst, R.J. (1979). *The interpretation of igneous rocks*. London, United Kingdom: Allen and Unwin, 450 p. <https://doi.org/10.1007/978-94-017-3373-1>
- Irvine, T.N., & Baragar, W.R.A. (1971). A guide to the chemical classification of the common volcanic rocks. *Canadian Journal of Earth Science*, 8(5), 523-548. <https://doi.org/10.1139/e71-055>
- Peccerillo, A., & Taylor, S.R. (1976). Geochemistry of Eocene calc-alkaline volcanic rocks from the Kastamonu area, Northern Turkey. *Contributions to Mineralogy and Petrology*, (58), 63-81. <https://doi.org/10.1007/BF00384745>
- Chappell, B.W., & White, A.J.R. (1974). Two contrasting granite types. *Pacific Geology*, (8), 173-174.
- Pearce, J.A., Harris, N.B., & Tindle, A.G. (1984). Trace element discrimination diagrams for the tectonic interpretation of granitic rocks. *Journal of Petrology*, 25(4), 956-983. <https://doi.org/10.1093/petrology/25.4.956>
- Maniar, P.D., & Piccoli, P.M. (1989). Tectonic discrimination of granitoids. *Geological Society of America Bulletin*, 101(5), 635-643. [https://doi.org/10.1130/0016-7606\(1989\)101<0635:TDOG>2.3.CO;2](https://doi.org/10.1130/0016-7606(1989)101<0635:TDOG>2.3.CO;2)
- Pettijohn, F.J., Potter, P.E., & Siever, R. (1973). *Sand and sandstones*. New York, United States: Springer Verlag, 583 p. <https://doi.org/10.1007/978-1-4615-9974-6>
- Herron, M.M. (1988). Geochemical classification of terrigenous sands and shales from core or log data. *Journal of Sedimentary Research*, 58(5), 820-829. <https://doi.org/10.1306/212F8E77-2B24-11D7-8648000102C1865D>
- Bracciali, L., Marroni, M., Pandolfi, L., & Rocchi, S. (2007). Geochemistry and petrography of Western Tethys Cretaceous sedimentary covers (Corsica and Northern Apennines): From source areas to configuration of margins. *Geological Society of America Special Paper*, (420), 73-93. [https://doi.org/10.1130/2006.2420\(06\)](https://doi.org/10.1130/2006.2420(06))
- Roser, B.P., & Korsch, R.J. (1988). Provenance signatures of sandstone-mudstone suites determined using discriminant function analysis of major-element data. *Chemical Geology*, 67(1-2), 119-139. [https://doi.org/10.1016/0009-2541\(88\)90010-1](https://doi.org/10.1016/0009-2541(88)90010-1)
- Bhatia, M.R. (1983). Plate tectonics and geochemical composition of sandstones. *The Journal of Geology*, 91(6), 611-627. <https://doi.org/10.1086/628815>
- Mahdy, A.I. (1999). *Petrological and geochemical studies on the younger granites and Hammamat sediments at G-V uranium occurrence, Wadi Bali, North Eastern Desert, Egypt*. M.Sc. Thesis. Cairo, Egypt: Ain Shams University.
- Shalaby, M.H. (1996). Structural controls of uranium mineralizations at Gabal Qattar, North Eastern Desert, Egypt. *Proceedings of the Egyptian Academy of Sciences*, (46), 521-536.
- Webster, R., & Oliver, M.A. (2007). *Geostatistics for environmental scientists*. Chichester, United Kingdom: John Wiley & Sons, 317 p. <https://doi.org/10.1002/9780470517277>
- Mustafa, M.R., Rezaur, R.B., Saiedi, S., & Isa, M.H. (2012). River suspended sediment prediction using various multilayer perceptron neural network training algorithms – A case study in Malaysia. *Water Resources Management*, (26), 1879-1897. <https://doi.org/10.1007/s11269-012-9992-5>
- Shalaby, M.H., (1996). New occurrence of uranium mineralizations, G-VII, Gabal Qattar Uranium prospect, North Eastern Desert, Egypt. *Bulletin of the Faculty of Science, Assiut University*, 35(2), 447-460.
- El Zalaky, M.A. (2002). *In interplay of plutonism, faulting, and mineralization, Northern Gabal Qattar peripheral zone, North Eastern Desert, Egypt*. M.Sc. Thesis. Benha, Egypt: Benha University, 178 p.
- Nesbitt, H.W., & Young, G.M. (1984). Prediction of some weathering trends of plutonic and volcanic rocks based on thermodynamic and kinetic considerations. *Geochimica et Cosmochimica Acta*, 48(7), 1523-1534. [https://doi.org/10.1016/0016-7037\(84\)90408-3](https://doi.org/10.1016/0016-7037(84)90408-3)
- Nesbitt, H.W., & Young, G.M. (1989). Formation and diagenesis of weathering profiles. *The Journal of Geology*, 97(2), 129-147. <https://doi.org/10.1086/629290>
- Saber, E.S.A. (2020). Gold resources from clastic Cambrian rocks and their link with underlying Precambrian rocks, Southern Sinai, Egypt. *Arabian Journal of Geosciences*, (13), 529. <https://doi.org/10.1007/s12517-020-05526-0>
- Saber, E.S., Ali, M., & El-Sheikh, A. (2018). Provenance studies of Kalabsha kaolin deposits, Egypt: A petrographical and geochemical approach. *Arabian Journal of Geosciences*, (11), 339. <https://doi.org/10.1007/s12517-018-3690-4>
- Meyer, C., & Hemley, J.J. (1967). Wall rock alteration. *Geochemistry of Hydrothermal Ore Deposits*, 166-232.
- Le Maitre, R.W., Bateman, P., Dubek, A., Keller, J., & Lameyre, J. (1989). *A classification of igneous rocks and glossary of terms: Recommendations of the International Union of Geological sciences sub-commission on the systematics of igneous rocks*. Oxford, United Kingdom: Black-Well Scientific Publications.

- [39] Large, R.R., Allen, R.L., Blake, M.D., & Herrmann, W. (2001). Hydrothermal alteration and volatile element halos for the Rosebery K lens volcanic-hosted massive sulfide deposit, Western Tasmania. *Economic Geology*, 96(5), 1055-1072. <https://doi.org/10.2113/gsecongeo.96.5.1055>
- [40] Cuney, M. (2009). The extreme diversity of uranium deposits. *Mineralium Deposita*, (44), 3-9. <https://doi.org/10.1007/s00126-008-0223-1>
- [41] Cuney, M., & Kyser, K. (2008). Recent and not-so-recent developments in uranium deposits and implications for exploration. *Mineralogical Association of Canada Short Course Series*, (39), 258.
- [42] Mahdy, N.M. (2011). *Mineralogical studies and mineral chemistry of some radioactive mineralizations in Gabal Gattar Area, Northern Eastern Desert, Egypt*. Ph.D. Thesis. Cairo, Egypt: Ain Shams University.
- [43] Large, R.R., Gemmill, J.B., Paulick, H., & Huston, D.L. (2001). The alteration box plot: A simple approach to understanding the relationship between alteration mineralogy and lithochemistry associated with volcanic-hosted massive sulfide deposits. *Economic Geology*, 96(5), 957-971. <https://doi.org/10.2113/96.5.957>
- [44] Wilde, A., Otto, A., Jory, J., MacRae, C., Pownceby, M., Wilson, N., & Torpy, A. (2013). Geology and mineralogy of uranium deposits from Mount Isa, Australia: Implications for albitite uranium deposit models. *Minerals*, 3(3), 258-283. <https://doi.org/10.3390/min3030258>

Геологічний та геостатистичний аналіз еквівалентної уранової і торієвої мінералізації, Східна пустеля Гаттар-V, Єгипет

Е.С.А. Сабер, А. Ісмаель, А. Ембабі, Є.З. Дарвіш, С.М. Селім, Е. Гомаа, А.А. Арафат

Мета. Оцінка розподілу уранової та торієвої руди для створення карти потенціалу урану та оцінки запасів уранової руди в районі Гаттар-V, Східна пустеля, Єгипет.

Методика. Для визначення еквівалентного уранового оруднення на ділянці Гаттар-V застосовано мультидисциплінарний підхід, що включає геологічні (петрографічні, мінералогічні та геохімічні) та геостатистичні (крігінг-аналіз та моделі варіограм) методи. Геостатистичний метод використовується для вивчення динаміки зміни та розподілу U і Th у більш молодих гранітах, так і в осадових відкладеннях Хаммамату. Значення Total Gamma, eU та eTh використовуються в крігінг-аналізі та моделях варіограм для визначення їхньої просторової залежності та виконання просторової інтерполяції розріджених вимірювань та карти рівня відкладень.

Результати. Встановлено, що уранове оруднення, розташоване вздовж або поблизу контакту молодших гранітів з осадовими відкладеннями Хаммамату, виявляє зміни епісієнітизації та знебарвлення відповідно. Встановлено сильний взаємозв'язок між урановим орудненням та індексом хімічної зміни (ІХЗ), особливостями зміни порід за складом та пов'язаною з цим мінералізацією гідротермальних розчинів.

Наукова новизна. Надано кількісну оцінку просторового розташування таких геологічних об'єктів, як уранове оруднення на основі застосування мультидисциплінарного методу, що поєднує петрографічні, мінералогічні та геохімічні дослідження з геостатистичним аналізом.

Практична значимість. Моделі варіограм та крігінг-аналіз також можна використовувати для оцінки літологічного складу гірських порід та мінералогічних фаз, а також вони дають чітке уявлення про розподіл елементів у руді, що дуже корисно на етапах планування та видобування.

Ключові слова: Гаттар-V, уранове оруднення, зміни за складом, гідротермальний, крігінг-аналіз, моделі варіограм